Construction and Building Materials 220 (2019) 712–726

Contents lists available at ScienceDirect

Construction and Building Materials

journal homepage: www.elsevier.com/locate/conbuildmat

Special Issue
CICE 2018 - FRP composites in construction: Advances in material research & engineering

Width effect of interfacial bond characteristics

Yu-Fei Wu [a,*,1], Liang He [b,2,3]

[a] School of Engineering, RMIT University, Australia
[b] Guangzhou Metro Design and Research Institute Corporation Limited, China

HIGHLIGHTS

- Factors affecting the size effect is rationally analysed.
- Experimental tests involving DIC is used to study the width effect.
- Width effect varies along bond length and interfacial fracture energy is width dependent.
- Width effect is modelled through rational reasoning and regression of test results.
- New factor is included in bond model.

ARTICLE INFO

Article history:
Received 8 March 2019
Received in revised form 9 May 2019
Accepted 13 June 2019
Available online 24 June 2019

Keywords:
Composite structure
Interface
Bond
Size effect
Width effect
Fracture mode

ABSTRACT

The bond properties of an interface in composite structures are generally considered as local mechanical characteristics. Through experimental testing and analytical study, it is shown in this work that the interfacial bond characteristics are generally size dependent, which involve both Mode II and Mode III fractures. For fiber-reinforced polymer (FRP) externally bonded (EB) to concrete members, this size effect is called the width effect. Test results in this work show that there is a central region on EB FRP-to-concrete bond face where only Mode II fracture is involved, and hence, the bond properties are size independent. The measured bond test results in the central region are used to determine interfacial bond properties that are size independent. The global test results or overall bond responses are subsequently used to determine the width effect and its model, through rational reasoning and regression of test results. The proposed model includes new factor that has not been considered in the width effect modeling, and consequently shows a better performance.

1. Introduction

Interfacial bonding connects substrates of different types of materials, by adhesion, friction or mechanical interlocking. The stress and strain fields at the bond interface, involving bonding agent and the local vicinity of connected parts of substrates, are usually much more complicated than those in other parts of a structure. To avoid such complexity and facilitate the application of conventional structural theories to composite structures, a convenient and sensible approach is to lump all additional deformations that cannot be included in conventional structural theory (such as beam theory) into a concentrated displacement at the interface, namely, interfacial slip. The interaction between the connected substrates is subsequently simplified into a resistance to the interfacial slip by a bond-slip relationship which can be identified from bond tests or pull-off tests for a particular type of interfacial joint. Such an ingenious treatment of bond interface converts a highly complicated problem into one within the regime of conventional mechanics and forms the cornerstone of modern composite mechanics.

Due to the concentration of interfacial deformation in the small vicinity surrounding an interface, the bond-slip relationship is often considered as local, related only to the material and geometric properties of bonding agent and material properties of connected substrates. As the interfacial slip includes the deformation

* Corresponding author.
E-mail address: yufei.wu@rmit.edu.au (Y.-F. Wu).
[1] Formerly, Dept. of Architecture and Civil Engineering, City University of Hong Kong, Hong Kong Special Administrative Region.
[2] Formerly M.Sc. student at Hunan University, Changsha, Hunan Province, China.
[3] Formerly research assistant, Dept. of Architecture and Civil Engineering, City University of Hong Kong, Hong Kong Special Administrative Region.

https://doi.org/10.1016/j.conbuildmat.2019.06.106
0950-0618/

Nomenclature

b_c	width of concrete block	s	local slip
b_f	width of FRP sheet	s_m	maximum elastic slip of bi-linear load-slip curve
b_{fo}	width of FRP without width effect	t_f	thickness of FRP sheet
E_f	elastic modulus of FRP sheet	*Theo*	theoretical value
Expe	experimental value	α	a parameter controlling the bond-slip relationship
f_{co}	concrete compressive strength	β	a parameter controlling the bond-slip relationship
f_t	concrete tensile strength	Δx	incremental distance used for calculation of bond stress
G_f	fracture energy	ε	longitudinal strain of FRP sheet
K_0	initial stiffness of load- slip curve	η	a coefficient given by Eq. (12)
L	bond length	κ_L	factor related to bond length L
L_e	effective bond length	κ_w	width factor
P	pull load	τ	bond stress
P_u	maximum pull load	τ_{max}	maximize bond stress

of not only the bonding agent but also the surrounding substrate materials, from structural mechanics point of view (by magnifying the vicinity of bond region to the size of a macroscopic building structure) the reaction of the structure to a certain value of interfacial slip, i.e. bond resistance, is not only related to the deformability of the bonding agent but also that of the substrates. The substrate deformation can be considered as a structural deformation problem, which is related to the geometry of the structure. Therefore, strictly speaking interfacial bond is related to the domain of substrates or structural size, and hence, is size dependent. In other words, the local nature of bond-slip relationship is conditional, e.g. in the case of infinitely large substrates with infinite bond interface.

For a joint as shown in Fig. 1 where a reinforcing material A is bonded to substrate B, both the deformation of the bonding agent and that of substrate B contribute to the interfacial slip. The interfacial shear movement causes stresses not only in the substrate material directly below the bonded area (such as point Q under the bonding agent) but also pushes against the surrounding substrate material outside the boundary of the bond area (such as point P). In other words, the surrounding material also takes part in resisting the interfacial shear movement. When the bond area is large, the surrounding material has little effect to the bond resistance in the central part of the bond area. When the bond area becomes smaller or approaches zero, the resistance to slip caused by the substrate material directly under the bond area reduces and diminishes (because the material under the bonded area diminishes) and that by the surrounding substrate material increases quickly. Due to this additional restraint from the surrounding material, the bond-slip relationship for the local area at the boundary of a bond area is much stiffer than that inside, as concluded in [1]. This boundary effect to bond-slip relationship is related to the size of the bond area, and hence, is not local but size dependent.

On the other hand, the stiffness of reinforcing material A also has a significant effect on the bond-slip relationship. Assuming the stiffness of material A is zero, a concentrated slip at a particular point of material A only causes the movement of a small local area in substrate B. For the reason given above, this bond resistance is larger due to the relatively larger effect of the surrounding material to this local slip. If the stiffness of material A is infinite and the bond area is very large, a translational slip at a particular point of the reinforcing material causes the slip of the whole of material A together. In this case, each unit area of material A is resisted only by the same area of material in substrate B directly beneath it, and the effect of surrounding substrate material outside the bond area is equally shared by the large bond area and approaches zero asymptotically when the bond area approaches infinity. Therefore, the bond resistance (for unit bond area) in this case is smaller. From this point of view, the interfacial bond-slip relationship is also related to the stiffness of the reinforcing material A.

On a two-dimensional interface such as concrete beams reinforced with externally bonded (EB) steel or fiber-reinforced polymer (FRP) plates, this size effect is referred to as the width effect [2–4]. The interfacial bond properties of such composite beams are affected by the width of the attached plate b_f relative to the width of the beam b_c (Fig. 2). Numerous models have been developed to consider the width effect on bond properties of EB-steel or

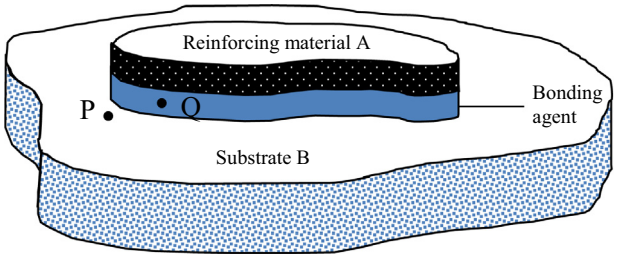

Fig. 1. Bond interface.

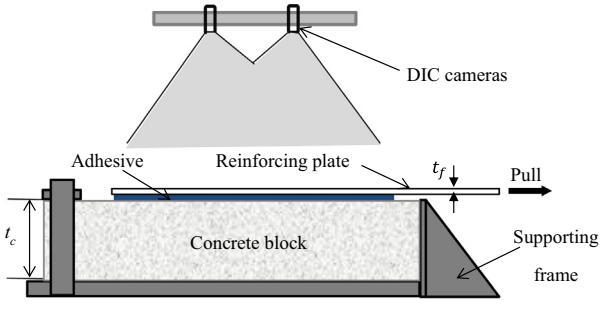

(a) Side view

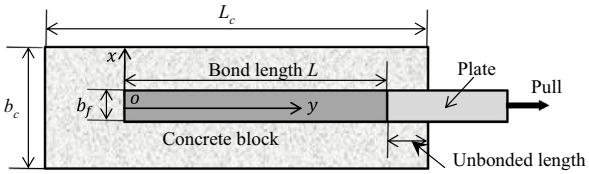

(b) Plane view

Fig. 2. Pull-off test.

EB-FRP reinforced beams [2,4–7]. However, the existing models for the width effect so far are not only significantly inconsistent [8] but also theoretically flawed. For example, only b_f/b_c is considered in most width effect models. Based on the discussions above, it is clear that more factors affect this width effect.

In this paper, Digital Image Correlation (DIC) was used to capture the strain field of FRP sheet externally bonded to a concrete block. A new approach is used to investigate the width effect. Through rational analytical studies of the measured strain fields, the width effect is identified and quantified, from which a new model is developed for engineering use.

2. Experimental tests

Pull-off tests are currently the conventional means for investigating interfacial bond properties [8–21]. The more popular single

Table 1
Test specimens and results.

Specimen ID	$E_f t_f$ (GPa·mm)	f_{co} (MPa)	L (mm)	b_f (mm)	b_c (mm)	α (mm)	β (mm)
C20-30-1	41.5	25.3	30	50	150	0.0803	18.6
C20-50-1	41.5	25.3	50	50	150	0.0927	19.2
C20-100-1	41.5	25.3	100	50	150	0.0969	18.6
C20-250-1	41.5	25.3	250	50	150	0.0895	19.3
C20-30-2	81.7	25.3	30	50	150	0.0828	25.5
C20-50-2	81.7	25.3	50	50	150	0.0834	25.5
C20-100-2	81.7	25.3	100	50	150	0.0867	25.8
C20-250-2	81.7	25.3	250	50	150	0.0884	25.4
C20-400-2	81.7	25.3	400	50	150	0.0941	26.5
C20-30-3	119.3	25.3	30	50	150	0.0798	30.2
C20-50-3	119.3	25.3	50	50	150	0.0813	30.7
C20-100-3	119.3	25.3	100	50	150	0.0718	30.7
C20-250-3	119.3	25.3	250	50	150	0.0875	31.7
C30-30-1	41.5	32.9	30	50	150	0.0820	17.1
C30-50-1	41.5	32.9	50	50	150	0.0833	16.8
C30-100-1	41.5	32.9	100	50	150	0.0918	16.5
C30-250-1	41.5	32.9	250	50	150	0.0939	17.1
C30-30-2	81.7	32.9	30	50	150	0.0818	25.2
C30-50-2	81.7	32.9	50	50	150	0.0844	25.1
C30-100-2	81.7	32.9	100	50	150	0.0867	23.8
C30-250-2	81.7	32.9	250	50	150	0.0938	24.3
C30-400-2	81.7	32.9	400	50	150	0.0907	24.8
C30-30-3	119.3	32.9	30	50	150	0.0913	29.8
C30-50-3	119.3	32.9	50	50	150	0.0925	29.8
C30-100-3	119.3	32.9	100	50	150	0.0756	28.5
C30-250-3	119.3	32.9	250	50	150	0.0753	29.1
C40-30-1	41.5	43.1	30	50	150	0.0757	15.8
C40-50-1	41.5	43.1	50	50	150	0.0765	16.2
C40-100-1	41.5	43.1	100	50	150	0.0847	15.9
C40-250-1	41.5	43.1	250	50	150	0.0825	16.1
C40-30-2	81.7	43.1	30	50	150	0.0789	23.2
C40-50-2	81.7	43.1	50	50	150	0.0834	23.6
C40-100-2	81.7	43.1	100	50	150	0.0881	22.6
C40-250-2	81.7	43.1	250	50	150	0.0771	23.5
C40-400-2	81.7	43.1	400	50	150	0.0815	23.4
C40-30-3	119.3	43.1	30	50	150	0.0821	28.1
C40-50-3	119.3	43.1	50	50	150	0.0763	28.3
C40-100-3	119.3	43.1	100	50	150	0.0866	27.4
C40-250-3	119.3	43.1	250	50	150	0.0833	26.8
C50-30-1	41.5	46.1	30	50	150	0.0866	16.9
C50-50-1	41.5	46.1	50	50	150	0.0899	16.0
C50-100-1	41.5	46.1	100	50	150	0.0770	15.7
C50-250-1	41.5	46.1	250	50	150	0.0910	16.4
C50-30-2	81.7	46.1	30	50	150	0.0935	21.5
C50-50-2	81.7	46.1	50	50	150	0.0779	23.4
C50-100-2	81.7	46.1	100	50	150	0.0790	21.6
C50-250-2	81.7	46.1	250	50	150	0.0881	22.9
C50-400-2	81.7	46.1	400	50	150	0.0750	23.5
C50-30-3	119.3	46.1	30	50	150	0.0843	26.7
C50-50-3	119.3	46.1	50	50	150	0.0860	27.2
C50-100-3	119.3	46.1	100	50	150	0.0769	27.0
C50-250-3	119.3	46.1	250	50	150	0.0926	27.4
C60-30-1	41.5	59.0	30	50	150	0.0784	14.5
C60-50-1	41.5	59.0	50	50	150	0.0787	14.8
C60-100-1	41.5	59.0	100	50	150	0.0820	15.9
C60-250-1	41.5	59.0	250	50	150	0.0818	15.9
C60-30-2	81.7	59.0	30	50	150	0.0912	20.8
C60-50-2	81.7	59.0	50	50	150	0.0834	21.5
C60-100-2	81.7	59.0	100	50	150	0.0838	22.0
C60-250-2	81.7	59.0	250	50	150	0.0737	22.2
C60-400-2	81.7	59.0	400	50	150	0.0744	21.2
C60-30-3	119.3	59.0	30	50	150	0.0893	25.5
C60-50-3	119.3	59.0	50	50	150	0.0724	26.3
C60-100-3	119.3	59.0	100	50	150	0.0776	26.2
C60-250-3	119.3	59.0	250	50	150	0.0861	27.1

pull-off test [8,11,13–17,19,21] was adopted in the bond tests in this work (Fig. 2). A total of 65 specimens were tested in the Heavy Structure Testing Laboratory at City University of Hong Kong. The concrete blocks used for the pull-off tests had the dimensions of 150 mm (width) × 150 mm (depth) × L_c (length), where L_c = 300, 450, or 600 mm, for bond lengths of L = 30–100, 250 and 400 mm, respectively. Details of the test specimens are given in Table 1. The test variables involved: (1) concrete strength, includ-

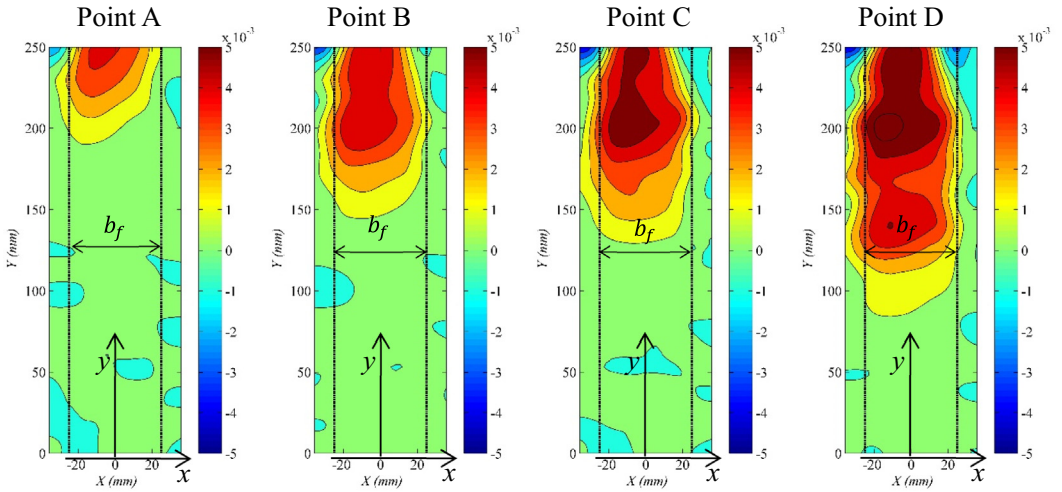

(a) Strain ε_{yy} in Y direction

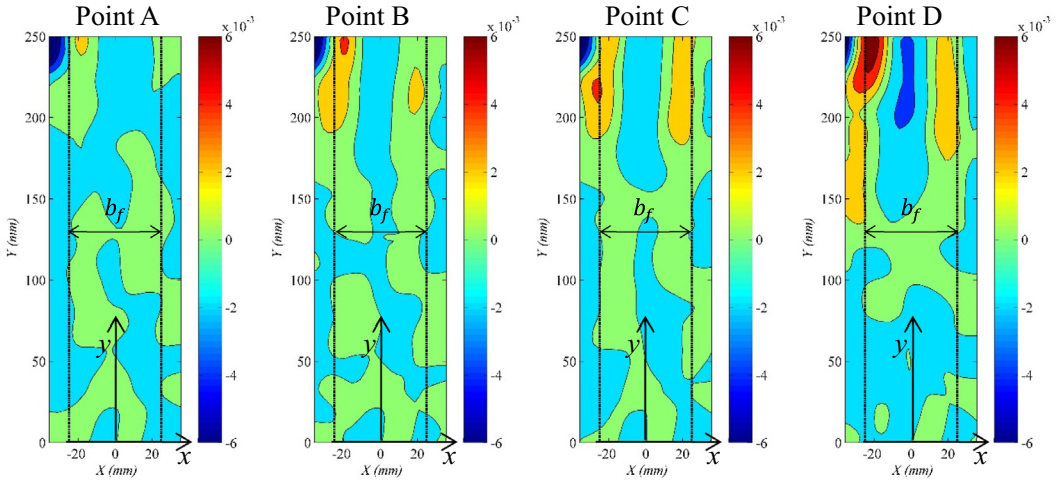

(b) Strain ε_{xx} in X direction

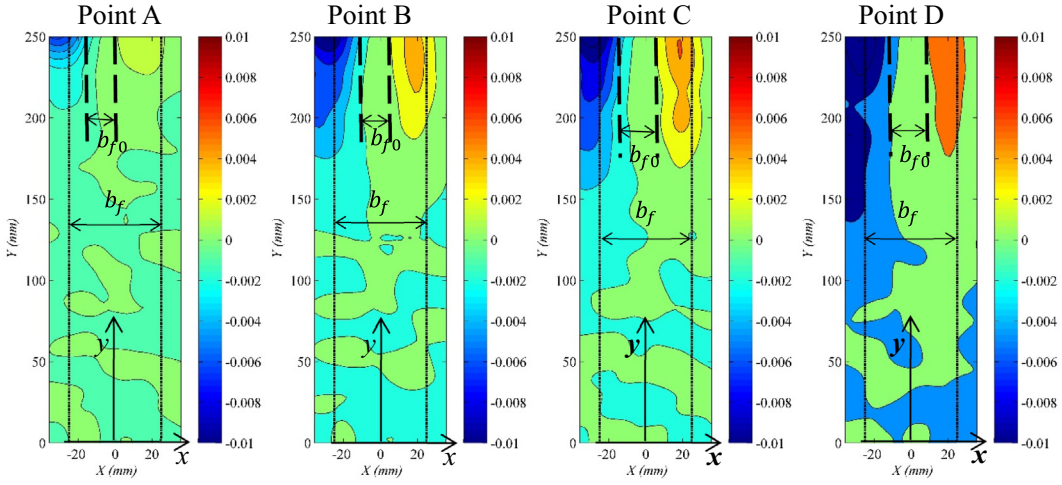

(c) Strain ε_{xy} in XY direction

Fig. 3. Strain distributions.

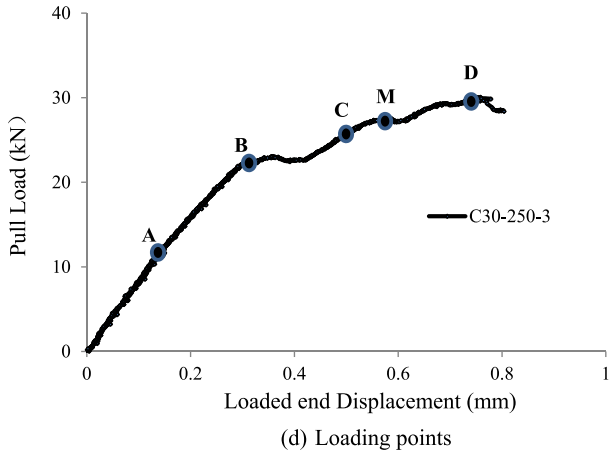

(d) Loading points

Fig. 3 (*continued*)

ing five grades of C20, C30, C40, C50, and C60; (2) bond length, being 30, 50, 100, 250, and 400 mm; and (3) stiffness of FRP sheet, with three variations of 1-, 2-, and 3-ply of carbon FRP (CFRP). The three parts of the specimen ID in Table 1 specifies concrete grade, bond length and FRP ply number, respectively. For example, C30-250-3 specifies concrete grade C30, bond length 250 mm and 3 plies of FRP. Tests were conducted under a displacement control mode at a very small displacement rate of 0.001–0.003 mm/s. A smaller rate was used for an expected more brittle failure mode. Preparation of specimens was similar as in [8]. The FRP material properties were determined by coupon tests in accordance with ASTM D3039/D3039M [22]. Concrete material properties were determined by compression tests in accordance with ASTM C39/C39M [23].

The displacement and strain fields on the surface of the test specimens were continuously captured by the DIC system (Fig. 2). DIC records the movement of particles on the surface of an object by digital cameras. By calculating the variation of relative position of different particles (image motion and distortions), strain components in any direction on the surface of an object can be obtained at any time. Compared with the traditional electrical strain gauge measurement, DIC can provide more detailed, continuous, accurate and reliable strain data and is particularly suitable for interfacial bond tests [24]. It has been proved to work very well by the authors' group in different kinds of experimental tests of concrete structures [8,24–27]. For the particular tests, the DIC images were captured at a frequency of 20 HZ using two cameras with 1280 × 1024 pixels. The strain accuracy was 0.025%. However, it is noted that DIC also has limited accuracy and care should be exercised in interpreting DIC results at very small displacement [28].

3. Strain distributions

The typical strain distributions of the FRP sheet for specimen C30-250-3 are shown in Fig. 3, where ε_{yy}, ε_{xx}, and ε_{xy} are the longitudinal, transverse and the shear strain, respectively. The dashed lines show the boundary of the FRP sheet. A few typical transverse and longitudinal sections of ε_{yy} distributions are shown in Fig. 4. The longitudinal strain distribution can be divided into three regions: (I) unstressed region; (II) stress transfer zone; and (III) fully debonded zone (Fig. 4b). Within the stress transfer zone, the strain distribution is increasing from the free end which is similar to previous observations [1]. In the fully debonded zone, the strains are approximately constant, slightly dropping from the boundary of region II and region III towards the loaded end. This phenomenon has been noted in experimental tests reported in the literature [12,29] but has puzzled researchers in the past. A rational explanation of the phenomenon was provided by He et al. [30] in a mathematical study and by others [31–34].

Fig. 4a shows that the longitudinal strain of FRP at a cross-section is not uniform which is consistent to the observation in [35]. This variation in the transverse direction (X direction) is the result of the width effect. In other words, in bond tests where there

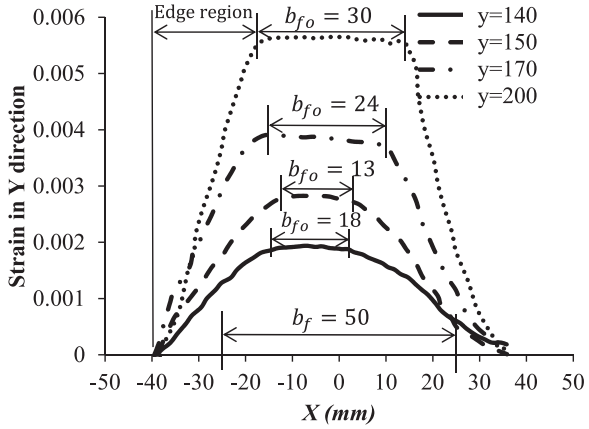

(a) ε_{yy} at different cross-sections

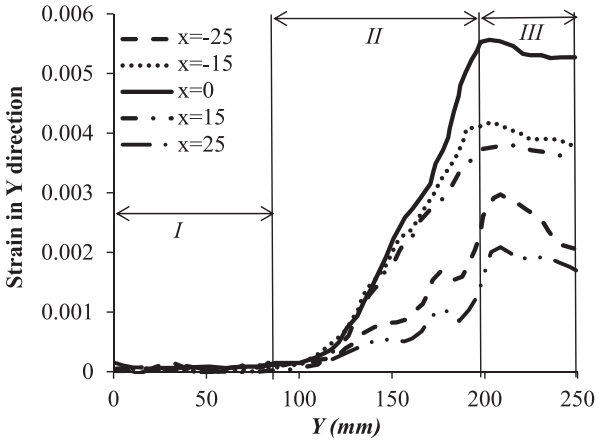

I= Unstressed region; II= Stress transfer zone; III= Fully debonded zone

(b) ε_{yy} at different x (location x refers to Fig. 4a)

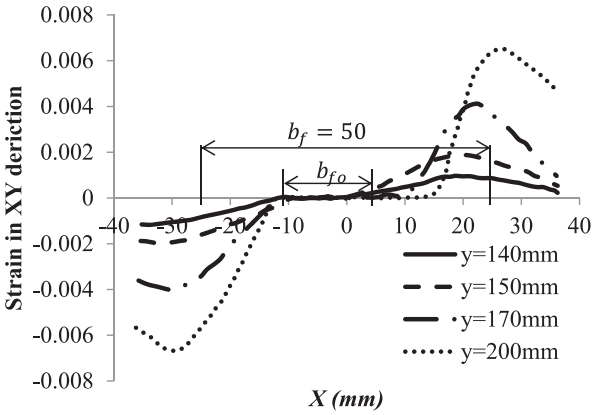

(c) ε_{xy} at different cross-sections

Fig. 4. Longitudinal strain distributions of specimen C30-250-3 at loading point *M* (Fig. 3d).

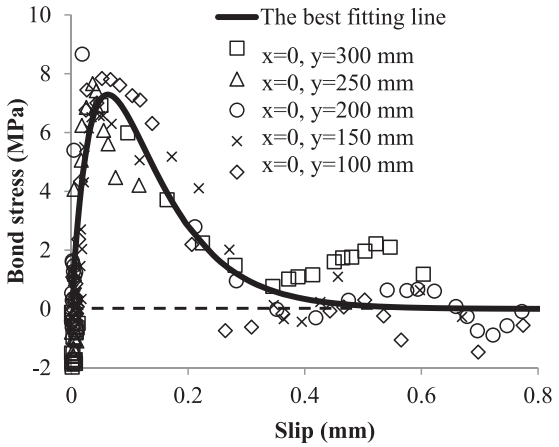

(a) Bond-slip curves without width effect

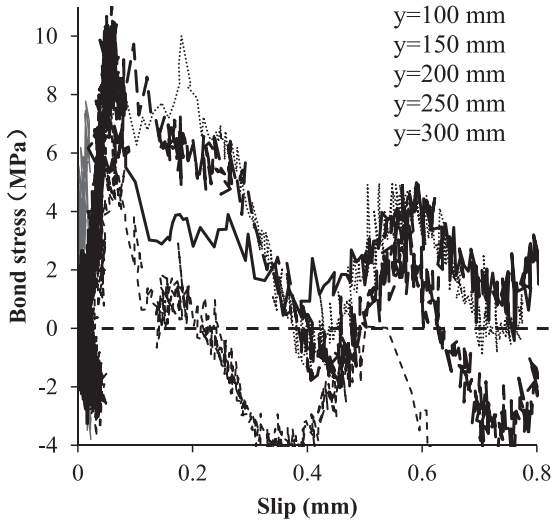

(b) Bond-slip curves with width effect

Fig. 5. Bond-slip curves of specimen C30-400-2 at different cross-sections.

is no width effect, the longitudinal strain across a cross-section should be uniform. The strain variation in a cross-section causes distortion of the FRP sheet and transverse shear strain. This can also be seen in Fig. 3c: the transverse shear strain is larger near the side of the FRP sheet, where the longitudinal strain is less uniform. In the meantime, there is a central region of width b_{fo} (Fig. 3c) where the shear strain is approximately zero. The longitudinal strains within b_{fo} are approximately constant (Fig. 4a). The regions of high transverse shear are referred to as edge region [35]. The edge regions extend from the side of central region within the FRP sheet to a point on concrete surface where longitudinal strain is zero (Fig. 4a). The transverse shear stress is significant in both the FRP sheet and the concrete in the edge regions, further outside which the transverse shear and axial strains are zero.

In the central region, the FRP strain and bond stress across the width direction are essentially uniform; and hence this does not involve the width effect. This analysis leads to the important conclusion that the bond properties derived from the central region do not involve the width effect. Furthermore, the crack front is perpendicular to the direction of loading in the central region [35]. Based on the definition of fracture mode, interfacial debonding in this central region belongs to Mode II fracture. The FRP in the edge regions is subjected to both transverse shear and longitudinal strains. Hence, the interfacial cracking in the edge regions involves Mode III fracture where the transverse shear stress is parallel to the crack front. In other words, debonding in the edge regions is a mix of Mode II and Mode III fractures [35]. This part of observations are generally consistent with those in [35]. However, it was concluded in [35] that "the dimension of the edge region was found to be approximately constant throughout the length of the stress transfer zone (STZ) (region II in Fig. 4b). Based on the results in Fig. 4(a), the width of the central region significantly varies along the bond length which shows a 3-dimentional nature of the width effect that brings in another important factor affecting the width effect (further discussion in Section 7).

4. Bond properties under pure Mode II fracture

The bond stress at a particular location of the interface can be calculated by Eq. (1) [30,31,36]:

$$\tau(y) = E_f t_f \frac{\varepsilon(y + \Delta y/2) - \varepsilon(y - \Delta y/2)}{\Delta y} \quad (1)$$

where E_f and t_f are the elastic modulus and thickness of the attached sheet, respectively; $\varepsilon(y)$ gives the strain of the attached sheet at location y and $\triangle y$ is an incremental length used for calculation of bond stress. A large value of $\triangle y$ gives an average bond stress in a region rather than a local one. A too small value of $\triangle y$ causes significant scattering of calculated results. Therefore, a reasonable balance between the two should be considered. A value of $\triangle y = 8$ mm was found reasonable [24] and is used in this work unless stated otherwise. The FRP strain distribution in the central region is used to calculate bond-slip curves in this section, where only Mode II fracture exists without the width effect. Typical

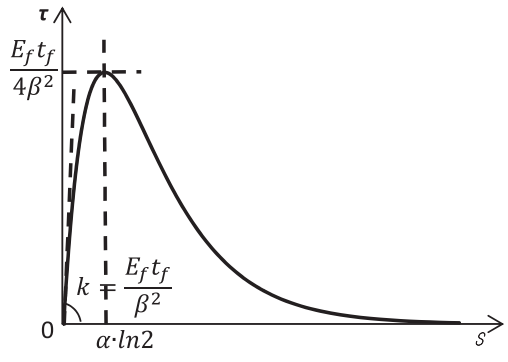

(a) Bond-slip model

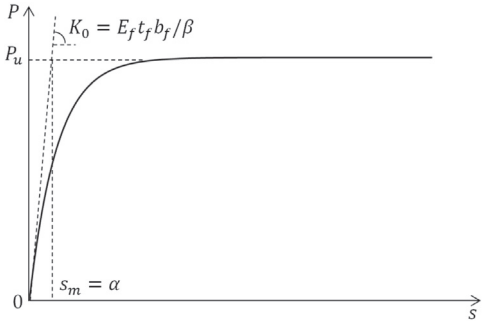

(b) Load-slip curve

Fig. 6. Bond model.

bond-slip curves calculated in this way are shown in Fig. 5 for specimen C30-400-2 at different locations. The slip values are obtained from DIC readings directly. It can be seen from Fig. 5a that the bond-slip curves at different locations in the central region are similar. Compared with the bond-slip curves reported in the literature which were measured by electrical strain gauges [9,10,13,17,29,37], these bond-slip curves are more stable and less scattered. The more stable and consistent results are due to more accurate and stable DIC measurements compared with those calculated from conventional closely spaced electrical strain gauges.

The bond-slip curves calculated from the average strain and slip of the FRP sheet at a whole cross-section are shown in Fig. 5b.

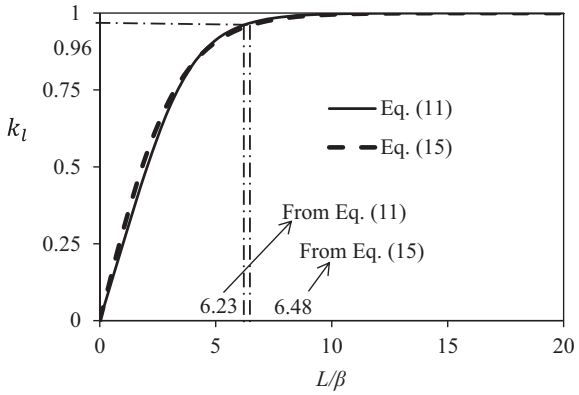

Fig. 7. Peak strength at different bond lengths.

These results are much more scattered compared with those in Fig. 5a. It can also be seen from Fig. 4a that the width of the central region changes at different cross-sections, which indicates that the width effect varies along the bond length. In other words, the average bond-slip curves at different cross-sections involve different width effects, and hence, should be different, as illustrated by Fig. 5b. Clearly, the bond-slip curves from the central region, where the fracture mode is pure Mode II, do not involve the width effect, and hence, should be used to calculate the bond-properties.

The popular bond-slip model as given by Eq. (2) [1,3,30,38] and shown in Fig. 6a is used to derive the interfacial bond parameters herein:

$$\tau(s) = \frac{E_f t_f \alpha}{\beta^2} e^{-s/\alpha}\left(1 - e^{-s/\alpha}\right) \tag{2}$$

where α and β are the two parameters that control the amplitude and shape of the bond-slip curve. The corresponding loaded-end slip vs. pull force curve obtained by integration of the bond-slip curve is shown in Fig. 6b. It can be seen from Fig. 6b that the reciprocal of β determines the initial slope K_0 of the load-slip curve and α is the slip at the turning point of the equivalent bilinear curve, or the peak elastic slip s_m [8].

Based on the definition of interfacial fracture energy and Eq. (2), one has:

$$G_f = \int_0^\infty \tau ds = \frac{E_f t_f \alpha^2}{2\beta^2} \tag{3}$$

The maximum bond stress (peak point in Fig. 6a) can be obtained from $d\tau/ds = 0$, which gives

Table 2
Outline of database.

Reference	N_1	N_2	f_{co} (MPa)	$E_f t_f$ (GPa·mm)	L (mm)	b_f (mm)	b_c (mm)	b_f/b_c
Chajes et al. [13]	16	15	24.0–47.1	110.2	50.8–203.2	25.4	152.4–228.6	0.11–0.17
Maeda et al. [53]	8	2	40.8–44.7	25.3–50.6	65–700	50	100	0.5
Takeo et al. [61]	33	33	24.1–49.3	25.5–115.2	100–500	40	100	0.4
Brosens and Van Gemert [43]	24	23	43.7	39.2–117.7	150–200	80–120	150	0.53–0.8
Kamiharako et al. [50]	18	11	34.9–75.5	13.5–60.0	100–200	10–90	100	0.1–0.9
Sato et al. [17]	20	2	23.8–43.4	25.3–122.8	65–700	10–200	100–500	0.1–0.67
Adhikary and Mutsuyoshi [41]	7	7	24.0–36.5	25.3–75.9	100–150	100	150	0.67
Bimal and Hiroshi [42]	7	7	24–36.5	25.5–76.8	100–150	100	150	0.67
Fu-quan et al. [74]	31	31	24.1–70.0	39.1–193	50–300	70	100	0.7
Nakaba et al. [54]	36	34	23.8–57.6	21.8–87.2	300	50	100	0.5
Wu et al. [21]	22	22	57.6	19.1–195	250–300	40–100	100	0.4–1
Dai et al. [46]	17	16	33.1–35	8.7–75.9	210–330	100	400	0.25
Tan [62]	12	10	29.3	16.4–32.8	300	50	100	0.5
Dai [47]	17	17	32.8–35	25.3–75.9	50–300	50–100	400	0.13–0.25
Kanakubo et al. [51]	12	12	23.8–57.6	20.3–87.2	300	50	100	0.5
Ren [57]	36	26	22.4–43.3	42.1–68.3	60–150	20–80	150	0.13–0.53
Ebead et al. [48]	32	32	42.5	25.0–58.4	50–320	25.4	150	0.17
Pham and Al-Mahaidi [56]	22	22	55.6	73.6–220.7	60–220	100	140	0.71
Dai et al. [3]	25	23	35	25.3–95.8	330	100	400	0.25
Yao et al. [29]	72	56	18.9–27.1	28.6–42.2	75–240	15–100	100–150	0.1–1
Ferracuti [49]	15	15	36.4–52.6	36.9–237	203–400	25–80	150–229	0.11–0.53
Sharma et al. [59]	18	18	29.7–35.8	198–360	100–300	50	100	0.5
Ko and Sato [52]	18	5	31.4	10.4–87.2	300	50	100	0.5
Subramaniam et al. [60]	13	13	39	38.4	150	12–46	125	0.096–0.368
Pellegrino et al. [55]	16	15	58.0–63.0	38.0–193.0	200–280	50	100	0.5
Savoia et al. [58]	23	23	26	40–216	100–400	80–100	150	0.53–0.67
Zhou [64]	123	123	45.6–65.4	12.3–40.1	20–200	15–150	150	0.1–1
Shi et al. [75]	12	12	27.1	12.7–52.7	230	50	100	0.5
Bilotta et al. [76]	18	16	19	174–309	300	60–100	160	0.375–0.625
Bilotta et al. [10]	34	34	21.5–26	38.2–238	50–400	50–100	150	0.5–0.67
Liu [77]	3	1	57.6	282.9	600	50	250	0.2
Czaderski and Olia [44]	8	8	32–33	203–286	300	100	150	0.67
Wu and Jiang [8]	65	65	25.3–59.02	41.5–119.3	30–400	50	150	0.33
Hunebum et al. [78]	17	16	27.7–31.4	175–294	300	60–100	150	0.4–0.67
Total	850	765	18.9–75.5	8.7–360	20–700	15–200	100–500	0.096–1

Note: N_1 = Specimen number in original reference, N_2 = Useful specimen number.

Table 3
Existing Bond-slip Models.

Reference	Bond-slip models
Neubauer and Rostasy [65]	$\tau = \begin{cases} \tau_{max} s/s_0 \text{ if } s \leqslant s_0 \\ 0 \text{ if } s > s_0 \end{cases}$, $\tau_{max} = 1.8\kappa_w f_t, s_0 = 0.202\kappa_w$, $\kappa_w = \sqrt{1.125\frac{2-b_f/b_c}{1+b_f/400}}$
Monti et al. [79]	$\tau = \begin{cases} \frac{s}{s_0}\tau_{max} \text{ if } s \leqslant s_0 \\ \frac{s_f - s}{s_f - s_0}\tau_{max} \text{ if } s > s_0 \end{cases}$, $\tau_{max} = 1.8\kappa_w f_t$, $s_0 = 2.5\tau_{max}\left(\frac{t_a}{E_a} + \frac{50}{E_c}\right)$, $s_f = 0.33\kappa_w$, $\kappa_w = \sqrt{1.125\frac{2-b_f/b_c}{1+b_f/400}}$
Nakaba et al. [54]	$\tau = \tau_{max}\frac{s}{s_0}\frac{3}{2+(s/s_0)^3}$, $\tau_{max} = 3.5f_c^{0.19}$, $s_0 = 0.051$
Savoia et al. [80]	$\tau = \tau_{max}\frac{s}{s_0}\frac{2.86}{2.86+(s/s_0)^{2.86}}$, $\tau_{max} = 3.5f_c^{0.19}$, $s_0 = 0.051$
Dai and Ueda [81]	$\tau = \begin{cases} \tau_{max} \times \left(\frac{s}{s_0}\right)^{0.575} \text{if } s \leqslant s_0 \\ \tau_{max} e^{-\beta(s-s_0)} \text{ if } s > s_0 \end{cases}$, $\tau_{max} = \frac{-1.575\alpha K_\alpha + \sqrt{2.481\alpha^2 K_\alpha^2 + 6.3\alpha\beta^2 K_\alpha G_f}}{2\beta} s_0 = \frac{\tau_{max}}{2K_\alpha}$, $\alpha = 0.028(E_f t_f)^{0.254}$, $\beta = 0.0035K_\alpha(E_f t_f)^{0.34}$, $K_\alpha = \frac{G_a}{t_a}G_f = 7.554K_\alpha^{-0.449}f_c^{0.343}$
Ueda et al. [82]	$\tau = 2BG_f(e^{-Bs} - e^{-2Bs})$, $B = 6.846(E_f t_f)^{0.108}(G_a/t_a)^{0.833}$, $G_f = 0.446(E_f t_f)^{0.023}(G_a/t_a)^{-0.352}f_{co}^{0.236}$
Lu et al. [4]	$\tau = \begin{cases} \tau_{max} \times \left(\frac{s}{s_0}\right)^{0.5} \text{ if } s \leqslant s_0 \\ \tau_{max} e^{-\alpha(s/s_0-1)} \text{ if } s > s_0 \end{cases}$, $\alpha = \left(\frac{G_f}{\tau_{max}s_0} - \frac{2}{3}\right)^{-1}$, $G_f = 0.308\kappa_w^2\sqrt{f_t}$, $\kappa_w = \sqrt{\frac{2.25-b_f/b_c}{1.25+b_f/b_c}}$
Wu and Jiang [8]	$\tau = \frac{E_f t_f \alpha}{\beta^2}e^{-s/\alpha}(1 - e^{-s/\alpha})$, $\alpha = 0.094f_{co}^{0.026}$, $\beta = \frac{0.134\sqrt{E_f t_f}}{\kappa_w f_{co}^{0.082}}$, $\kappa_w = 1 + 0.222f_{co}^{0.304}(1 - b_f/b_c)$
Pan and Wu [83]	$\tau = \begin{cases} ks \text{ if } s \leqslant s_0 \\ \tau_{max} e^{-\beta(s-s_0)} \text{ if } s > s_0 \end{cases}$, $\tau_{max} = 0.131\kappa_w^2 f_{co}^{0.19}$, $\kappa_w = 1 + 0.222f_{co}^{0.304}(1 - b_f/b_c)$
	$\beta = 5.304f_{co}^{-0.026}$, $\rho = \frac{A_f}{A_c}$, $k = \frac{G(1+\rho')A_f \tanh(\alpha L)}{\alpha t_f h}$, $\alpha = \sqrt{\frac{G}{ht_p}\frac{E_c - \rho E_f}{E_f E_c}}$
This work	$\tau = \frac{E_f t_f \alpha}{\beta^2}e^{-s/\alpha}(1 - e^{-s/\alpha})$, $\alpha = 0.124f_{co}^{-0.103}$, $\beta = 0.174f_{co}^{-0.205}(E_f t_f)^{0.5}$

$$\tau_{max} = \frac{E_f t_f \alpha}{4\beta^2} \text{ (when } s = \alpha \times \ln 2) \tag{4}$$

It is analytically concluded by Wu and Jiang [8] that α is affected only by the properties of concrete and hence can be expressed as a function of f_{co}, while β is a function of f_{co}, $E_f t_f$ and the width effect. As the bond parameters discussed in this section do not involve the width effect, β is only a function of f_{co} and $E_f t_f$. Therefore, α and β can be expressed by

$$\alpha = A f_{co}^B \tag{5}$$

$$\beta = C f_{co}^D (E_f t_f)^E \tag{6}$$

It is widely accepted in the literature that the interfacial fracture energy and the maximum bond stress are not related to $E_f t_f$ [3,4,6,10,16]. Substituting Eqs. (5) and (6) into Eq. (3) gives $G_f = A^2 f_{co}^{2B-2D} / \left[2C^2 (E_f t_f)^{2E-1}\right]$. To ensure G_f is not related to $E_f t_f$, the term 2E-1 must be equal to 0 which gives E = 0.5. The same result of E = 0.5 is obtained by substituting Eqs. (5) and (6) into Eq. (4).

Using the experimental bond-slip curves of a test specimen as illustrated in Fig. 5a, the values of α and β can be determined by regressing (best matching) Eq. (2) to the test curves. The values of α and β for all test specimens are calculated in this way and given in Table 1. Using the values of α and β given in Table 1 as a database, coefficients A, B, C and D in Eqs. (5) and (6) can be determined from regression analyses, which gives

$$\alpha = 0.124 f_{co}^{-0.103} \text{ (in N, mm)} \tag{7}$$

$$\beta = 0.174 f_{co}^{-0.205} (E_f t_f)^{0.5} \text{ (in N, mm)} \tag{8}$$

5. Bond properties involving Mode III fracture

Based on the analytical solution proposed by the authors [8,30,36], the bond strength of the joint with a finite bond length is given by

$$P_u(L) = \kappa_L \cdot P_u(\infty) \tag{9}$$

where $P_u(\infty)$ is the bond strength when the bond length L approaches infinity, or the maximum strength, given by

$$P_u(\infty) = E_f t_f b_f \frac{\alpha}{\beta} \tag{10}$$

and κ_L is a length factor relating the maximum strength to the bond strength of a joint with the bond length L, given by

$$\kappa_L = \frac{\eta\sqrt{1-\eta^2}\sinh\left(\sqrt{1-\eta^2}L/\beta\right)}{1 + \eta\cosh\left(\sqrt{1-\eta^2}L/\beta\right)} \tag{11}$$

in which η is a solution of the following equation

$$\begin{aligned} &2\eta^2\tfrac{L}{\beta}\sqrt{1-\eta^2}\cosh\left(\tfrac{L}{\beta}\sqrt{1-\eta^2}\right) - 2(1-2\eta^2)\sinh\left(\tfrac{L}{\beta}\sqrt{1-\eta^2}\right) \\ &+2\tfrac{L}{\beta}\eta^3\sqrt{1-\eta^2} + \eta^3\sinh\left(\tfrac{2L}{\beta}\sqrt{1-\eta^2}\right) = 0 \end{aligned} \tag{12}$$

Substituting Eq. (3) into Eq. (10) gives Eq. (13), which is identical to the well-known ultimate bond strength model based on fracture mechanics [3,7,39].

$$P_u(\infty) = b_f\sqrt{2G_f E_f t_f} \tag{13}$$

However, the analytical solutions of Eqs. (9)–(13) are for 2-D problems that ignore the width effect. The width effect can be allowed for by applying a width factor κ_w to Eq. (9), or

$$P_u(L) = E_f t_f b_f \frac{\alpha}{\beta}\kappa_L\kappa_w \tag{14}$$

Based on the discussions earlier, the width factor κ_w equals to 1 when only Mode II fracture is involved at the interface. When Mode III fracture occurs together with Mode II, κ_w is greater than 1 because the fracture energy of Mode III is about two times that of Mode II [40].

Bond tests normally involve the width effect unless widths of the bonded sheet and concrete substrate are equal. With α and β given by Eqs. (7) and (8) that do not involve the width effect, the width factor κ_w can be obtained by regressing Eq. (14) to the test results of $P_u(L)$. Detailed modeling of κ_L and κ_w is studied in the following sections.

Table 4
Existing Models of Bond Strength, Fracture Energy and Width Factor.

Reference	Bond strength	Fracture energy	Width factor
Van Gemert [37]	$P_u = 0.5 b_f L f_t$	NA	NA
Holzenkampfer [71]	$P_u = b_f \sqrt{G_f E_f t_f}$	$G_f = 0.204 f_t = 0.453 f_{co}^{0.55}$	NA
Tanaka [84]	$P_u = b_f L(6.13 - lnL)$	NA	NA
Hiroyuki and Wu [85]	$P_u = b_f L\left(5.88 L^{-0.669}\right)$	NA	NA
Maeda et al. [53]	$P_u = b_f L_e \tau_u$, $L_e = e^{6.13-0.58\ln(E_f t_f)}$ $\tau_u = 110.2 \times 10^{-6} E_f t_f$	NA	NA
Neubauer and Rostasy [65]	$P_u = \begin{cases} 0.64 \kappa_w b_f \sqrt{f_t E_f t_f} & \text{if } L \geqslant L_e \\ 0.64 \kappa_w b_f \sqrt{f_t E_f t_f} \frac{L}{L_e}\left(2 - \frac{L}{L_e}\right) & \text{if } L < L_e \end{cases}$, $L_e = \sqrt{\frac{E_f t_f}{2 f_t}}$	NA	$\kappa_w = \sqrt{1.125 \frac{2 - b_f/b_c}{1 + b_f/400}}$
Khalifa et al. [14]	$P_u = b_f L_e \tau_u$, $L_e = e^{6.13-0.58\ln(E_f t_f)}$, $\tau_u = 110.2 \times 10^{-6} E_f t_f \left(\frac{f_{co}}{42}\right)^{2/3}$	NA	NA
Chaallal et al. [86]	$P_u = 2.7 b_f L / \left(1 + t_f \sqrt[4]{\frac{E_f b_f}{4 E_f I_f t_a}} \tan 33^\circ\right)$	NA	NA
Niedermeier [6]	$P_u = \begin{cases} 0.78 b_f \sqrt{G_f E_f t_f} \text{ if } L \geqslant L_e \\ 0.78 b_f \sqrt{G_f E_f t_f} \frac{L}{L_e}\left(2 - \frac{L}{L_e}\right) \text{ if } L < L_e \end{cases}$, $L_e = \sqrt{\frac{E_f t_f}{4 f_t}}$	$G_f = 0.204 \kappa_w^2 f_t = 0.453 \kappa_w^2 f_{co}^{0.55}$	$\kappa_w = \sqrt{1.125 \frac{2 - b_f/b_c}{1 + b_f/400}}$
Yang et al. [87]	$P_u = \left(0.5 + 0.08 \sqrt{\frac{0.01 E_f t_f}{f_t}}\right) b_f L_e \tau_a$, $\tau_a = 0.5 f_t$, $L_e = 100$mm	NA	NA
Chen and Teng [2]	$P_u = \begin{cases} 0.427 \kappa_w b_f L_e \sqrt{f_{co}} \text{ if } L \geqslant L_e \\ 0.427 \kappa_w b_f L_e \sqrt{f_{co}} \sin\left(\frac{\pi L}{2 L_e}\right) \text{ if } L < L_e \end{cases}$, $L_e = \sqrt{\frac{E_f t_f}{\sqrt{f_{co}}}}$	NA	$\kappa_w = \sqrt{\frac{2 - b_f/b_c}{1 + b_f/b_c}}$
Izumo model [88]	$P_u = \begin{cases} \left(3.8 f_c^{2/3} + 15.2\right) L E_f b_f t_f \times 10^{-3} \text{ for CFRP} \\ \left(3.4 f_c^{2/3} + 69\right) L E_f b_f t_f \times 10^{-3} \text{ for AFRP} \end{cases}$	NA	NA
Sato model [88]	$P_u = (b_f + 7.4) L_e \tau_u$, $L_e = 1.89 (E_f t_f)^{0.4}$ $\tau_u = 2.68 \times 10^{-5} f_c^{0.2} E_f t_f$	NA	NA
Iso model [88]	$P_u = b_f L_e \tau_u$, $L_e = 0.125 (E_f t_f)^{0.57}$ $\tau_u = 0.93 f_{co}^{0.44}$	NA	NA
Dai et al. [3]	$P_u = \begin{cases} (b_f + 7.4)\sqrt{2 G_f E_f t_f} \text{ if } L \geqslant 100\text{mm} \\ b_f \sqrt{2 G_f E_f t_f} \text{ if } L < 100\text{mm} \end{cases}$	$G_f = 0.514 f_{co}^{0.236}$	NA
Lu et al. [4]	$P_u = \begin{cases} b_f \sqrt{2 G_f E_f t_f} & \text{if } L \geqslant L_e \\ b_f \sqrt{2 G_f E_f t_f} \frac{L}{L_e}\left(2 - \frac{L}{L_e}\right) & \text{if } L < L_e \end{cases}$, $a_0 = \frac{1}{\lambda_2} \sin^{-1}\left(0.99 \sqrt{\frac{s_f - s_0}{s_f}}\right)$, $s_f = \frac{2 G_f}{\tau_{max}}$ $\lambda_1 = \sqrt{\frac{\tau_{max}}{s_0 E_f t_f}}$, $\lambda_2 = \sqrt{\frac{\tau_{max}}{(s_f - s_0) E_f t_f}}$, $s_0 = 0.0195 \kappa_w f_t$, $\tau_{max} = 1.5 \kappa_w f_t$	$G_f = 0.308 \kappa_w^2 \sqrt{f_t} = 0.207 \kappa_w^2 f_{co}^{0.275}$	$\kappa_w = \sqrt{\frac{2.25 - b_f/b_c}{1.25 + b_f/b_c}}$
Wu et al. [7]	$P_u = \begin{cases} 0.585 \kappa_w b_f f_{co}^{0.1} (E_f t_f)^{0.54} \text{ if } L \geqslant L_e \\ 0.585 \kappa_w b_f f_{co}^{0.1} (E_f t_f)^{0.54} \left(\frac{L}{L_e}\right)^{1.2} \text{ if } L < L_e \end{cases}$, $L_e = 0.395 (E_f t_f)^{0.54} f_{co}^{-0.09}$	NA	$\kappa_w = \sqrt{\frac{2.25 - b_f/b_c}{1.25 + b_f/b_c}}$
Wu and Jiang [8]	$P_u = E_f t_f b_f \frac{\alpha}{\beta} \kappa_l$, $\kappa_l = \frac{\eta \sqrt{1-\eta^2} \sinh\left(\frac{\sqrt{1-\eta^2} L}{\beta}\right)}{1 + \eta \cosh\left(\frac{\sqrt{1-\eta^2} L}{\beta}\right)}$, $\alpha = 0.094 f_{co}^{0.026}$, $\beta = \frac{0.134 \sqrt{E_f t_f}}{\kappa_w f_{co}^{0.082}}$, $\eta = 4.11 e^{-0.3835 L/\beta} - 3.61 e^{-0.4454 L/\beta}$	$G_f = 0.247 \kappa_w^2 f_{co}^{0.216}$	$\kappa_w = 1 + 0.222 f_{co}^{0.304}\left(1 - \frac{b_f}{b_c}\right)$
This work	$P_u(L) = E_f t_f b_f \frac{\alpha}{\beta} \kappa_L \kappa_w$, $\alpha = 0.124 f_{co}^{-0.103}$ $\beta = 0.174 f_{co}^{-0.205} (E_f t_f)^{0.5}$, $\kappa_L = \tanh(0.3 L/\beta)$	$G_f = 0.254 f_{co}^{0.204}$	$\kappa_w = 1 + 6.313 f_{co}^{0.372}\left[(E_f t_f)^{-0.299} + 0.007\right](1 - b_f/b_c)^{2.139}$

6. Length factor

The length factor κ_L can be obtained from Eqs. (11) and (12). However, the direct use of these two equations is inconvenient for practical applications. Through mathematical study, a simple and sufficiently accurate equation for κ_L is obtained in [30], as given by

$$\kappa_L = \tanh\left(\frac{0.3L}{\beta}\right) \tag{15}$$

Fig. 7 compares Eq. (15) (dashed line) with Eq. (11) (solid line). Therefore, Eq. (15) is used in this work. Eq. (15) can be rewritten as

$$L = \beta \frac{a \tanh(\kappa_L)}{0.3} \tag{16}$$

For a bond strength that is a fraction of the maximum bond strength, or $\kappa_L P_u(\infty)$, the corresponding bond length is given by Eq. (16). The value of L calculated from Eq. (16) for a selected value of κ_L close to 1.0 is called the effective bond length L_e, and κ_L = 0.96 is a common value used by researchers [1,3,30]. Compared with the exact solution from Eq. (11), the error of L_e/β given by Eq. (16) is smaller than 5% when κ_L is equal to 0.96.

7. Width factor

Rearranging Eq. (14) gives

$$\kappa_w = \frac{P_u(L)\beta}{E_f t_f b_f \alpha \kappa_L} \tag{17}$$

Test results of $P_u(L)$ are collected from both extant literature [3,10,11,13,17,18,21,29,38,41–64] and the authors' own tests (Table 1) to form a database for calculation of κ_w, as summarized in Table 2. It contains 850 test results of EB-FRP bond tests. The concrete strength, FRP stiffness $E_f t_f$, bond length and the width ratio (b_f/b_c) vary between 18.9 and 75.5 MPa, 8.7–360 GPa·mm, 20 to 700 mm, and 0.096–1, respectively.

Test data may be scattered due to differences in material preparation, test setup, and test method which affect failure mode [45]. Therefore, screening of test results is important before they are used for model calibration. Careful screening of the database shows that 765 out of the 850 test specimens had adequate failure mode of interfacial fracture with a layer of concrete peeled off by FRP sheet. Other specimens failed by other failure modes such as adhesive-concrete bond interface failure (no concrete skin peeled off), concrete prism failure and plate tearing. Therefore, only 765 specimens are used in this work for regression analyses. Out of the 765 tests, 65 are from Table 1. This database is the largest compared to those reported in the literature at the time this regression was carried out. The values of κ_w calculated using the database are used to derive the model through regression analysis.

Existing models of κ_w are listed in Tables 3 and 4. Most models assume that κ_w is a function of b_f and b_c. Wu and Jiang [8] further included concrete strength as another parameter and proposed the following model for the width factor:

$$\kappa_w = 1 + 0.222 f_{co}^{0.304}(1 - b_f/b_c)\ (\text{in N, mm}) \tag{18}$$

The width effect can be visualized as a result of the following two mechanisms:

(1) As the movement (or strain) of FRP sheet in the central region is larger than those at the edge regions (Figs. 3 and 4), the width effect is caused by the restraining from the concrete outside FRP sheet against its movement. The slip (or strain) field (Fig. 4a) is similar to the speed distribution of water flow in a channel where the side of the channel drags the water to cause a speed gradient (shear strain). The side-restraining or dragging effect in a fluid (boundary effect) is influenced by the properties of the fluid (viscosity). Similarly, the width effect of the FRP-concrete interface is also affected by the properties of the substrate material that is related to concrete strength. The side dragging effect should be higher in case of stiffer materials. Therefore, κ_w should increase when f_{co} increases from this point of view.

(2) On the other hand, the dragging effect is not only related to the strain profile of FRP sheet at a certain transverse cross-section but also related to the longitudinal strain distribution that is reflected by the effective bond length L_e. This can be seen in Fig. 4a where different width effects are shown at different cross-sections. When $E_f t_f$ approaches infinity or f_{co} approaches zero, L_e approaches infinity (see Eqs. (16) and (8)). In this case, it is a two-dimensional side-dragging (uniform strain profile along longitudinal direction) without the three-dimensional dragging effect and hence gives a smaller value of κ_w. From this point of view, κ_w should reduce when $E_f t_f$ increases or f_{co} reduces.

Mechanism (1) above is namely "the boundary layer effect" and "restraint to the FRP sheet from the surrounding concrete" in [35,60]. Mechanism (2) identify a new factor affecting the width effect: $E_f t_f$, for the first time. The above analyses on the two mechanisms are consistent with those discussed in Section 1. Based on the above arguments, the calculation of κ_w should take the following form:

$$\kappa_w = 1 + f(f_{co}) \cdot g(E_f t_f) \cdot h(b_f, b_c) \tag{19}$$

where $f(f_{co})$, $g(E_f t_f)$, and $h(b_f, b_c)$ are functions of f_{co}, $E_f t_f$, and FRP and concrete widths, respectively. These functions are to be determined. Eq. (19) satisfies all of the mechanisms discussed above. Using the collected database and through regression analyses, these functions are determined to be:

$$f(f_{co}) = f_{co}^{0.385}\ (\text{in N, mm}) \tag{19a}$$

$$g(E_f t_f) = 8(E_f t_f)^{-0.25} + 0.01\ (\text{in N, mm}) \tag{19b}$$

$$h(b_f, b_c) = (1 - b_f/b_c)^{0.61}/(1 + 0.01 b_f^{1.5})\ (\text{in N, mm}) \tag{19c}$$

Substituting Eqs. (19a)–(19c) into Eq. (19) gives

$$\kappa_w = 1 + f_{co}^{0.385}\left[8(E_f t_f)^{-0.25} + 0.001\right](1 - b_f/b_c)^{0.61}/\left(1 + 0.01 b_f^{1.5}\right)\ (\text{in N, mm}) \tag{20}$$

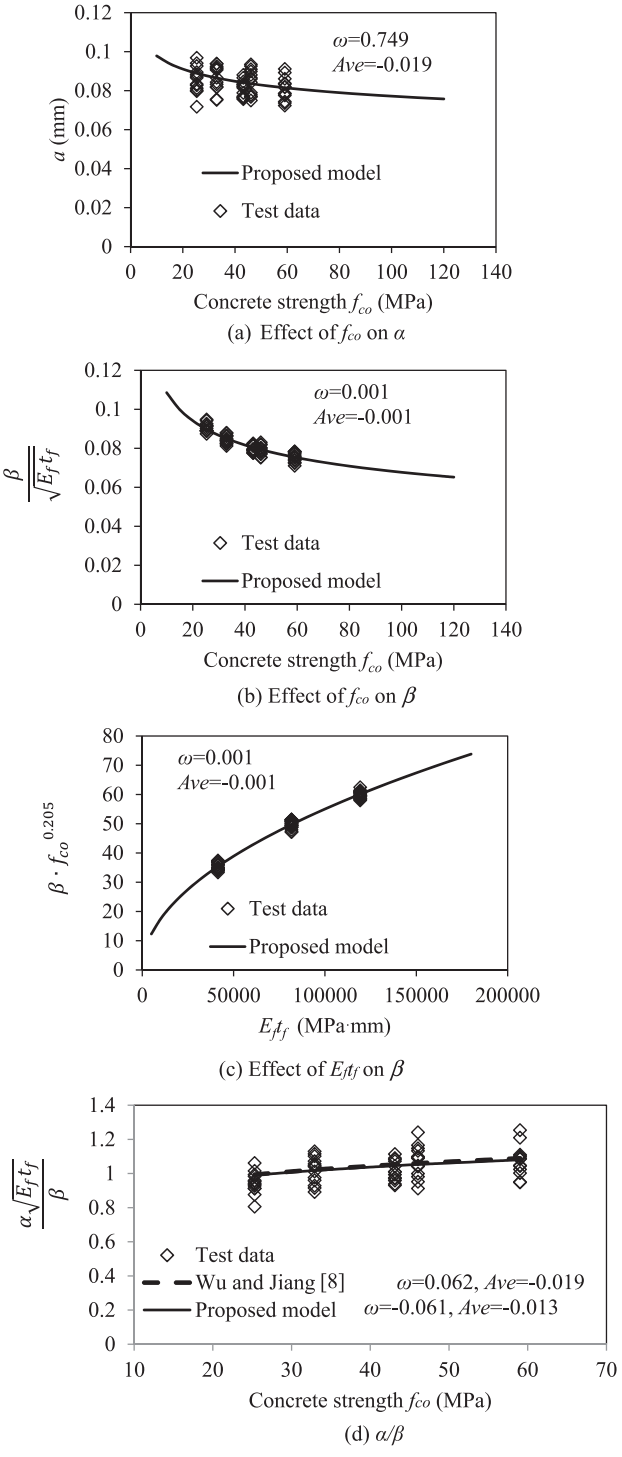

Fig. 8. Parameters α and β.

When b_f is equal to b_c, there is no width effect and the width factor is equal to 1.

8. Discussions

8.1. Parameters α and β

Comparisons between the experimentally obtained values of parameter α from the database in Table 1 and the model predictions are shown in Fig. 8a. The proposed model of α shows a slightly decreasing trend with the increase of f_{co}. Based on the analytical solution of Wu and Jiang [8], $\alpha = s_m = s_u$ (Fig. 6b) where s_u is the ultimate slip of a linear bond-slip model when the bond stress reaches its peak and suddenly drops to zero. Therefore, the value of α is related to the local slip capacity before debonding. For normal EB-FRP joints with a thin adhesive layer, the local slip capacity is closely related to deformability of the substrate material which is related to concrete grade. As the deformability of concrete decreases with the increase of concrete strength, the decreasing trend of α predicted by the new model is reasonable.

As shown in Fig. 6b, the reciprocal of β determines the initial slope K_0 of the load-slip curve. The β model (Eq. (8)) shows a decreasing tendency (meaning the initial slope K_0 increases) with the increase of concrete strength (Fig. 8b) and an increasing trend with the increase of FRP stiffness (Fig. 8c), both of which are also reasonable.

In Wu and Jiang [8], the bond strength is given by $P_u(L) = E_f t_f b_f \kappa_L \frac{\alpha}{\beta}$ where the width effect is included in β. Compared with Eq. (14), α/β in this work should be equivalent to $\alpha/(\beta\kappa_w)$ in Wu and Jiang [8]. These two ratios are compared in Fig. 8d between the proposed model and that by Wu and Jiang [8]. It can be seen from Fig. 8d that these two models are essentially the same for predicting the bond strength. As more factors are included in the new model of width effect, the new model could potentially perform better when more test data is available.

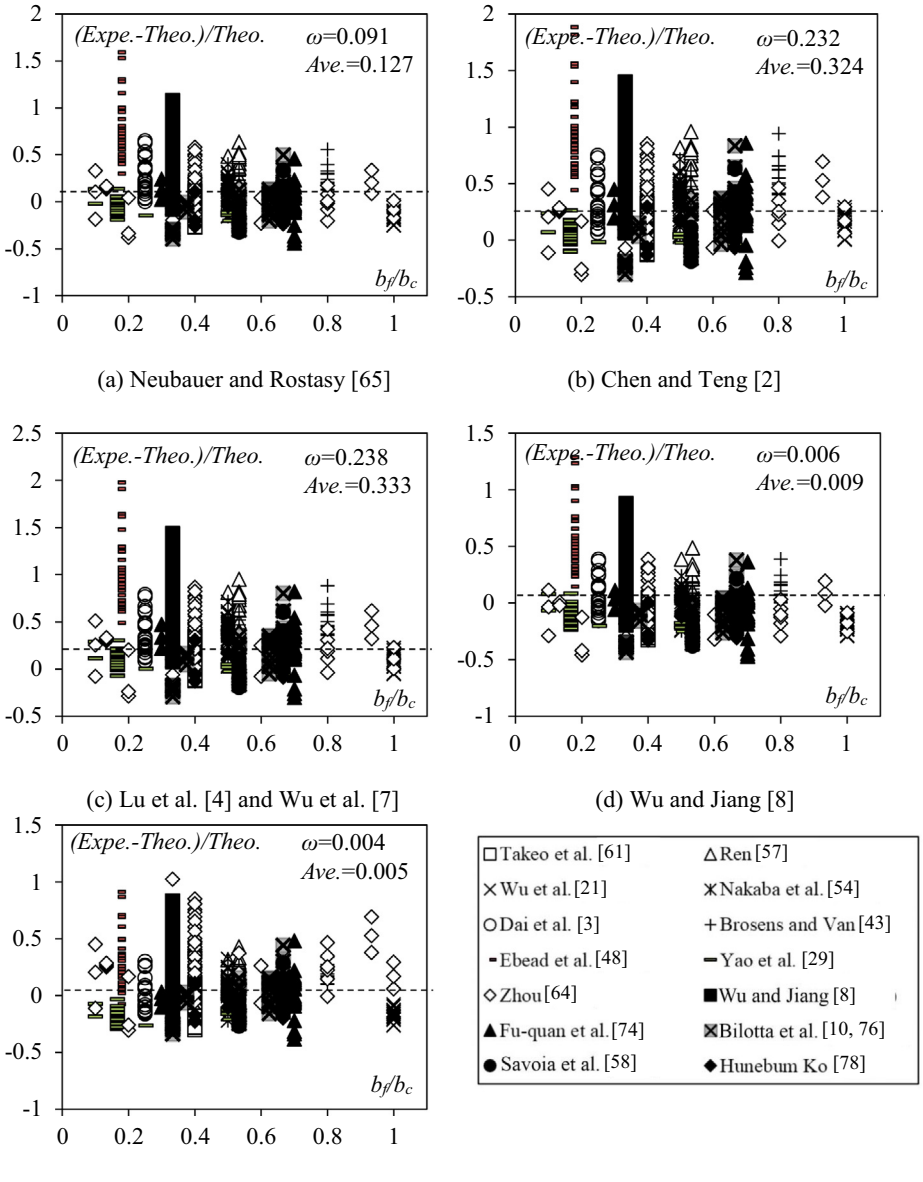

Fig. 9. Performance of k_w models.

8.2. Width effect

The models of the width effect reported in literature are listed in Table 3. The earlier models, such as those in [2,4,6,7,65], only considered b_f and b_c in the width effect. No model considers concrete strength as a factor of the width effect until Wu and Jiang [8]. The current study further extends the model of Wu and Jiang [8] by including another factor, the stiffness of FRP plate $E_f t_f$, into the width effect model.

Eq. (17) can be rewritten as

$$\kappa_w = \frac{\frac{P_u}{b_f}}{E_f t_f \frac{\alpha}{\beta} \kappa_L} = \frac{p_u}{E_f t_f \frac{\alpha}{\beta} \kappa_L} \tag{21}$$

where p_u is the bond strength for unit width of FRP plate. Therefore, Eq. (21) can be used to calculate the experimental value of k_w, where parameters α and β are given by Eqs. (7) and (8), respectively. The performance of the existing models and the proposed one (Eq. (20)) for k_w is compared with the test results calculated by Eq. (21) in Fig. 9 where Expe. and Theo. equal to experimental and theoretical results, respectively. The theoretical value of k_w for existing models are given by the equations in Table 3. For those that do not give $k_w = 1$ when $b_f/b_c = 1$, the k_w models should be scaled by a factor to make $k_w = 1$ when $b_f = b_c$ [8].

The performance of a model is evaluated with the following error index:

$$Err = \frac{Expe. - Theo.}{Theo.} \tag{22}$$

$$\omega = \frac{\sum |Expe. - Theo.|}{\sum |Theo.|} \tag{23}$$

$$Ave = \frac{\sum_{i=1}^{n} Err_i}{n} \tag{24}$$

Comparatively, the model proposed in this work gives a higher precision and smaller scattering ($\omega = 0.004$, $Ave. = 0.005$) among all the models. A relatively large scattering of results still exists in Fig. 9. This kind of error is largely caused by scattering of the test result itself and is difficult to avoid. As shown in Fig. 10, the test results from an identical design of specimen reported in the same work still show a large scattering.

8.3. Bond strength

The accuracy of the proposed bond strength model (Eq. (14)) and the existing ones is evaluated with error index ω and *Ave*. The results of the error analysis are shown in Fig. 11. For reasons similar to those discussed in the previous section, bond strengths show a relatively high scattering, regardless of the accuracy of a model. All of the existing models have a higher accuracy for the bond strength in the lower half of the range in Fig. 11. It is because most of the test results are in this region and the previous models were regressed using a database with test results in this region. Neubauer and Rostasy [65], Wu et al. [7] and Wu and Jiang [8] give a significantly larger value for bond strength in the upper half of the range, while Chen and Teng [2] and Lu et al. [4] provide a smaller one. Due to the inclusion of more parameters in modeling in this work, the performance of the proposed model is relatively better compared with others with the smallest error index $\omega = 0.164$.

8.4. Fracture energy

Substituting Eqs. (7) and (8) into Eq. (3) gives:

$$G_f = \frac{E_f t_f \alpha^2}{2\beta^2} = 0.254 f_{co}^{0.204} \text{ (in N, mm)} \tag{25}$$

Eq. (25) is suitable for 2D problems without consideration of the width effect. When the width effect is included in the fracture energy G_f, Eq. (13) gives the maximum bond strength considering

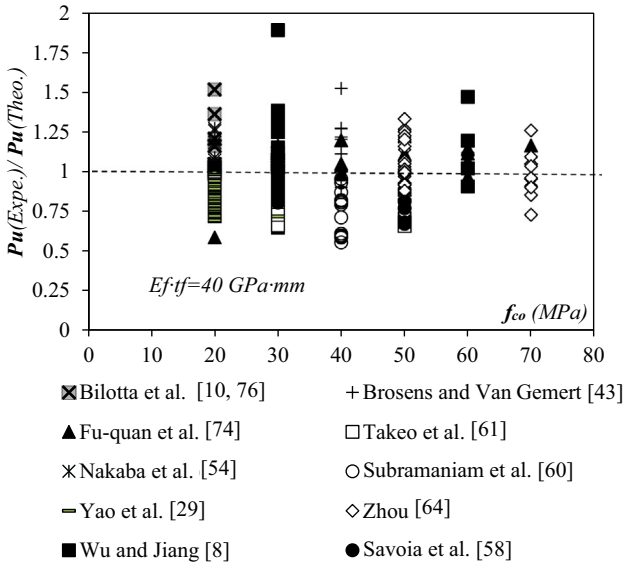

Fig. 10. Inconsistency of test results for identical test specimens.

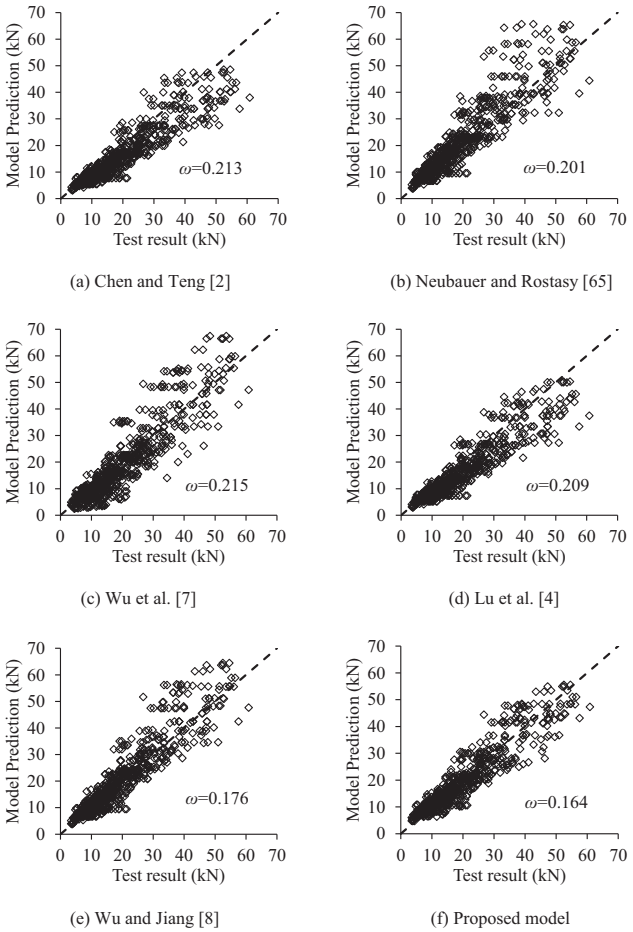

(a) Chen and Teng [2] (b) Neubauer and Rostasy [65]

(c) Wu et al. [7] (d) Lu et al. [4]

(e) Wu and Jiang [8] (f) Proposed model

Fig. 11. Performance of peak strength models.

the width effect and $P_u(L) = P_u(\infty)\kappa_L$ gives that with a limited bond length L. Substituting Eqs. (13) and (14) into the right and left sides of $P_u(L) = P_u(\infty)\kappa_L$, respectively, gives

$$G_f = \frac{E_f t_f \alpha^2}{2\beta^2}(\kappa_w)^2 = 0.254 f_{co}^{0.204}(\kappa_w)^2 \ (\text{in N, mm}) \quad (26)$$

κ_w is equal to 1 in a 2D problem, and hence, Eq. (25) is a special case of Eq. (26).

The width effect in the fracture energy of the debonding problem is actually similar to the size effect in fracture mechanics. For fracture of concrete, Bažant and Pfeiffer [66] showed that the fracture energy has no size effect for infinitely large specimens (no boundary effect). However, many researchers observed a size effect in fracture tests [67–70]. Different reasons have been given to explain the size effect in fracture tests, including inaccuracy of test [69], misconduct of test curve [70], and non-uniform crack propagation along ligament length [67,68].

Comparing the 2D fracture energy of Eq. (25) with the 3D one of Eq. (26), the non-uniform cracking field in a 3D problem is certainly a factor that causes the size effect in fracture energy. The existing models of fracture energy for the debonding problem are provided in Table 4. Holzenkampfer [71] proposed a model $G_f = 0.453 f_{co}^{0.55}$(in N, mm) which has the same form as Eq. (25) but different coefficients. A similar model of $G_f = 0.514 f_{co}^{0.236}$ (in N, mm) was proposed by Dai et al. [3]. Clearly, these two models exclude the width (size) effect. The fracture energy model developed by Niedermeier [6], Lu et al. [4] and Wu and Jiang [8] have the same form as Eq. (26). Therefore, the width effect is included in their models. The difference in the coefficients of different models is apparently caused by the use of different database for model regression.

It is controversial to include size effect in the fracture energy as it is considered in fracture mechanics as a material property that is not affected by size or geometry of an object. However, it is well known that the fracture energy is different for different fracture modes (Modes I, II, III, and mixed mode). It is also clear that geometry of the problem significantly affects stress condition (distribution and proportion of stress components) and consequently the fracture mode [35] (e.g. it is mode II fracture when there is no width effect and mode III fracture is involved when width effect exists). As a result, the fracture energy that is defined as the energy required to completely debond for unit bond area is naturally related to the size or width effect. In fact, the fracture criteria and fracture energy for mixed mode fracture are found to be related to loading or stress conditions [72,73].

9. Conclusions

The size effect of interfacial bond is investigated through experimental and analytical studies in this work. A new model for the width effect of EB FRP-to-concrete joints is developed. Although the experimental results were based on, and the developed models are applicable to, EB FRP-to-concrete joints only, the perception and analytical approach to the problem are general and applicable to interfacial bonds between different materials. The following observations and conclusions can be made from this work:

1. Strictly and generally speaking, interfacial bond is non-local and size dependent. For one-dimensional structural members such as beams and columns, the size effect is reflected by the width effect of bond.
2. This work supplements the important findings in [35] and further confirms (i) when only pure Mode II fracture is involved in interfacial shear bond, there is no width effect. It is the presence of Mode III fracture that causes the width effect; and (ii) there is a region in the center of an externally bonded reinforcing strip that has a uniform longitudinal strain. Bond properties derived from this central region do not involve the width effect.
3. The width effect varies along the bond length. In other words, average bond-slip relationship at different cross-sections involves different width effects.
4. The width effect is comparable to the dragging to water flow by the side of an open channel. Based on this analogy, a new factor affecting the width effect is identified and included into the proposed model. The coefficients of the proposed model are determined through regression analyses using a large test database. The proposed model shows an improved accuracy compared with other existing models.
5. When the width (size) effect is involved in bond, the interfacial fracture energy is width (size) dependent.

Declaration of Competing Interest

None.

Acknowledgement

Students Cheung Wing Chong, Gai Chao, Wong Lai Shan and Zhao Ming Xin took part in the experimental works. The work described in this paper was supported by the National Natural Science Foundation of China (Grant No. 51378449).

References

[1] Y.W. Zhou, Y.F. Wu, Y.C. Yun, Analytical modeling of the bond-slip relationship at FRP-concrete interfaces for adhesively-bonded joints, Compos. B Eng. 41 (6) (2010) 423–433.
[2] J.F. Chen, J.G. Teng, Anchorage strength models for FRP and steel plates bonded to concrete, J. Struct. Eng. 127 (7) (2001) 784–791.
[3] J.G. Dai, T. Ueda, Y. Sato, Development of the nonlinear bond stress–slip model of fiber reinforced plastics sheet–concrete interfaces with a simple method, J. Compos. Constr. 9 (1) (2005) 52–62.
[4] X.Z. Lu, J.G. Teng, L.P. Ye, J.J. Jiang, Bond–slip models for FRP sheets/plates bonded to concrete, Eng. Struct. 27 (6) (2005) 920–937.
[5] J.G. Dai, T. Ueda, Y. Sato, Unified analytical approaches for determining shear bond characteristics of FRP-concrete interfaces through pullout tests.", J. Adv. Concr. Technol. 4 (1) (2006) 133–145.
[6] R. Niedermeier, Envelope Line of Tensile Forces while Using Externally Bonded Reinforcement. PhD thesis, TU München, Germany, 2000 (In German).
[7] Z.S. Wu, S. Islam, H. Said, A three-parameter bond strength model for FRP–concrete interface, J. Reinf. Plast. Compos. 28 (19) (2009) 2309–2323.
[8] Y.F. Wu, C. Jiang, Quantification of bond-slip relationship for externally bonded FRP-to-concrete Joints, J. Compos. Constr. 17 (5) (2013) 673–686.
[9] M. Ali-Ahmad, K. Subramaniam, M. Ghosn, Experimental investigation and fracture analysis of debonding between concrete and FRP sheets, J. Eng. Mech. 132 (9) (2006) 914–923.
[10] A. Bilotta, M.D. Ludovico, E. Nigro, FRP-to-concrete interface debonding: Experimental calibration of a capacity model, Compos. B Eng. 42 (6) (2011) 1539–1553.
[11] L. Bizindavyi, K. Neale, Transfer lengths and bond strengths for composites bonded to concrete, J. Compos. Constr. 3 (4) (1999) 153–160.
[12] P. Carrara, D. Ferretti, F. Freddi, G. Rosati, Shear tests of carbon fiber plates bonded to concrete with control of snap-back, Eng. Fract. Mech. 78 (15) (2011) 2663–2678.
[13] M.J. Chajes, W.W. Finch, T.F. Januszka, T.A. Thomson, Bond and force transfer of composite-material plates bonded to concrete, ACI Struct. J. 93 (2) (1996) 208–217.
[14] A. Khalifa, W.J. Gold, A. Nanni, A.A. Mi, Contribution of externally bonded FRP to shear capacity of RC flexural members, J. Compos. Constr. 2 (4) (1998) 195–202.
[15] C. Mazzotti, M. Savoia, B. Ferracuti, A new single-shear set-up for stable debonding of FRP–concrete joints, Constr. Build. Mater. 23 (4) (2009) 1529–1537.
[16] J.L. Pan, C.K. Leung, Effect of concrete composition on FRP/concrete bond capacity, J. Compos. Constr. 11 (6) (2007) 611–618.
[17] Y. Sato, Y. Asano, T. Ueda, Fundamental study on bond mechanism of carbon fiber sheet, J. Mater., Concr. Struct. Pavements 47 (2000) 71–87 (In Japanese).
[18] J. Shi, H. Zhu, Z. Wu, R. Seracino, G. Wu, Bond behavior between basalt fiber–reinforced polymer sheet and concrete substrate under the coupled effects of freeze-thaw cycling and sustained load, J. Compos. Constr. 17 (4) (2013) 530–542.

[19] H. Toutanji, P. Saxena, L. Zhao, T. Ooi, Prediction of interfacial bond failure of FRP–concrete surface, J. Compos. Constr. 11 (4) (2007) 427–436.
[20] S.K. Woo, Y. Lee, Experimental study on interfacial behavior of CFRP-bonded concrete, KSCE J. Civ. Eng. 14 (3) (2010) 385–393.
[21] Z.S. Wu, H. Yuan, H. Yoshizawa, T. Kanakubo, Experimental/analytical study on interfacial fracture energy and fracture propagation along FRP-concrete interface, Proc., ACI Int. (2001) 133–152.
[22] ASTM D3039, D3039M, Standard test method for tensile properties of polymer matrix composite materials, American Society of Testing and Materials, West Conshohocken, PA, 1995.
[23] ASTM C39, C39M, Standard Test Method for Compressive Strength of Cylindrical Concrete Specimens, American Society of Testing and Materials, West Conshohocken, PA, 2011.
[24] Y.F. Wu, L. He, L.C. Bank, Bond-test protocol for plate-to-concrete interface involving all mechanisms, J. Compos. Constr. 20 (1) (2016) 04015022.
[25] C. Jiang, Y.F. Wu, G. Wu, Plastic hinge length of FRP-confined square RC columns, J. Compos. Constr. 18 (4) (2014) 04014003.
[26] Y.F. Wu, J.F. Jiang, Effective strain of FRP for confined circular concrete columns, Compos. Struct. 95 (2013) 479–491.
[27] Y.C. Yun, Y.F. Wu, Durability of CFRP–concrete joints under freeze–thaw cycling, Cold Reg. Sci. Technol. 65 (3) (2011) 401–412.
[28] H. Biscaia, N. Franco, C. Chastre, Stainless steel bonded to concrete: an experimental assessment using the DIC technique, Int. J. Concr. Struct. Mater 12 (2018) 9.
[29] J. Yao, J. Teng, J. Chen, Experimental study on FRP-to-concrete bonded joints, Compos. B Eng. 36 (2) (2005) 99–113.
[30] L. He, Y.F. Wu, Y. Xiao, Analytical solution for externally bonded joints considering snap-Back, J. Compos. Constr. 19 (5) (2015) 04014077.
[31] H. Yuan, J.G. Teng, R. Seracino, Z.S. Wu, J. Yao, Full-range behavior of FRP-to-concrete bonded joints, Eng. Struct. 26 (5) (2004) 553–565.
[32] H. Biscaia, I.S. Borba, C. Silva, C. Chastre, A nonlinear analytical model to predict the full-range debonding process of FRP-to-parent material interfaces free of any mechanical anchorage devices, Compos. Struct. 138 (2016) 52–63.
[33] J.G. Teng, H. Yuan, J.F. Chen, FRP-to-concrete interfaces between two adjacent cracks: Theoretical model for debonding failure, Int. J. Solids Struct. 43 (18–19) (2006) 5750–5778.
[34] P. Cornetti, A. Carpinteri, Modelling the FRP-concrete delamination by means of an exponential softening law, Eng. Struct. 33 (6) (2011) 1988–2001.
[35] K.V. Subramaniam, C. Carloni, L. Nobile, An understanding of the width effect in FRP–concrete debonding, Strain 47 (2) (2011) 127–137.
[36] Y.F. Wu, X.S. Xu, J.B. Sun, C. Jiang, Analytical solution for the bond strength of externally bonded reinforcement, Compos. Struct. 94 (11) (2012) 3232–3239.
[37] D. Van Gemert, Force transfer in epoxy bonded steel/concrete joints, Int. J. Adhes. Adhes. 1 (2) (1980) 67–72.
[38] K. Liu, Y.F. Wu, Analytical identification of bond–slip relationship of EB-FRP joints, Compos. B Eng. 43 (4) (2012) 1955–1963.
[39] B. Täljsten, Defining anchor lengths of steel and CFRP plates bonded to concrete, Int. J. Adhes. Adhes. 17 (4) (1997) 319–327.
[40] D. Lockner, J. Byerlee, V. Kuksenko, A. Ponomarev, A. Sidorin, Quasi-static fault growth and shear fracture energy in granite, Nature 350 (6313) (1991) 39–42.
[41] B.B. Adhikary, H. Mutsuyoshi, Study on the bond between concrete and externally bonded CFRP sheet, in: Proc., 5th International Symposium on Fiber Reinforced Polymer Reinforcement for Reinforced Concrete Structures, World Scientific, Singapore, 2001, pp. 371–378.
[42] B.A. Bimal, M. Hiroshi, Study on the Bond between Concrete and Externally Bonded CFRP Sheet, in: 5th International Symposium on FRP Reinforcement for Concrete Structures, University of Cambridge, Cambridge, 2001, pp. 371–378.
[43] K. Brosens, D. Van Gemert, Anchorage Design for Externally Bonded Carbon Fiber Reinforced Polymer Laminates SP-188, in: Proc., 4th Int. Symp. on Fiber Reinforced Polymer Reinforcement for Reinforced Concrete Structures, American Concrete Institute, Farmington Hills, MI, 1999, pp. 635–645.
[44] C. Czaderski, S. Olia, En-core Round Robin Testing Program–Contribution of Empa, Proc., the Sixth International Conference on FRP Composites in Civil Engineering, CICE, 2012.
[45] T. D'Antino, C. Pellegrino, Bond between FRP composites and concrete: Assessment of design procedures and analytical models, Compos. Part B 60 (2014) 440–456.
[46] J. Dai, Y. Sato, T. Ueda, Improving the load transfer and effective bond length for FRP composites bonded to concrete, Proc. Jpn. Concr. Inst. 24 (1) (2002) 1423–1428.
[47] J.G. Dai, Interfacial models for fiber reinforced polymer (FRP) sheets externally bonded to concrete PhD thesis, Hokkaido University, Hokkaido, Japan, 2003.
[48] U.A. Ebead, K.W. Neale, L. Bizindavyi, On the Interfacial Mechanics of FRP-Strengthened Concrete Structures, in: R. Seracino (Ed.), Proc., Proc., 2nd Int. Conf. on FRP Composites in Civil Engineering (CICE), Balkema Publications, Rotterdam Netherlands, 2004, pp. 351–359.
[49] B. Ferracuti, Strengthening of RC structures by FRP: experimental analyses and numerical modelling PhD thesis, University of Bologna, Italy, 2006.
[50] A. Kamiharako, T. Shimomura, K. Maruyama, H. Nishida, Analysis of bond and debonding behavior of continuous fiber sheet bonded on concrete, J. Mater. Constr. Struct. Pavement 634 (45) (1999) 197–208.
[51] T. Kanakubo, T. Furuta, H. Fukuyama, Bond strength between fiber-reinforced polymer laminates and concrete, in: Proc., 6th Int. Symp. on FRP Reinforcement for Concrete Structures FRPRCS-6, World Scientific, Singapore, 2003, pp. 133–142.
[52] H. Ko, Y. Sato, Bond stress–slip relationship between FRP sheet and concrete under cyclic load, J. Compos. Constr. 11 (4) (2007) 419–426.
[53] T. Maeda, Y. Asano, Y. Sato, T. Ueda, Y. Kakuta, A study on bond mechanism of carbon fiber sheet., in: Proc., 3rd Int. Symp. on Non-metallic (FRP) Reinforcement for Concrete Structures, Japan Concrete Institute, Tokyo, 1997, pp. 279–286.
[54] K. Nakaba, T. Kanakubo, T. Furuta, H. Yoshizawa, Bond behavior between fiber-reinforced polymer laminates and concrete, ACI Struct. J. 98 (3) (2001) 359–367.
[55] C. Pellegrino, D. Tinazzi, C. Modena, Experimental study on bond behavior between concrete and FRP reinforcement, J. Compos. Constr. 12 (2) (2008) 180–189.
[56] H. Pham, R. Al-Mahaidi, Bond characteristics of CFRP fabrics bonded to concrete members using wet lay-up method, in: R. Seracino (Ed.), Proc., 2nd Int. Conf. on FRP Composites in Civil Engineering (CICE-2004), Balkema Publications, Rotterdam, Netherlands, 2004, p. 407.
[57] H.T. Ren, Study on Basic Theories and Long Time Behavior of Concrete Structures Strengthened by Fiber Reinforced Polymers. PhD thesis, Dalian University of Technology, Dalian, China, 2003 (in Chinese).
[58] M. Savoia, A. Bilotta, F. Ceroni, M. Di Ludovico, G. Fava, B. Ferracuti, C. Mazzotti, E. Nigro, R. Olivito, M. Pecce, Experimental round robin test on FRP concrete bonding, in: 9th international Symposium on Fiber Reinforced Polymer Reinforcement for Concrete Structures, World Scientific, Singapore, 2009, pp. 13–15.
[59] S. Sharma, M.M. Ali, D. Goldar, P. Sikdar, Plate–concrete interfacial bond strength of FRP and metallic plated concrete specimens, Compos. B Eng. 37 (1) (2006) 54–63.
[60] K.V. Subramaniam, C. Carloni, L. Nobile, Width effect in the interface fracture during shear debonding of FRP sheets from concrete, Eng. Fract. Mech. 74 (4) (2007) 578–594.
[61] K. Takeo, H. Matsushita, T. Makizumi, G. Nagashima, Bond characteristics of CFRP sheets in the CFRP bonding technique, Proc. of Japan Concr. Inst. 19 (2) (1997) 1599–1604.
[62] Z. Tan, Experimental Research for RC Beam Strengthened with GFRP. MSc thesis, Tsinghua Univ., Beijing, China, 2002. in Chinese.
[63] F.Q. Xu, Y. Chen, J. Guan, in: Bond Strength between CFRP Sheets and Concrete, Elsevier Science, England, 2001, pp. 357–364.
[64] Y.W. Zhou, Analytical and Experimental Study on the Strength and Ductility of FRP-Reinforced High Strength Concrete Beam PhD thesis, Dalian University of Technology, Dalian, China, 2009.
[65] U. Neubauer, F.S. Rostasy, Design aspects of concrete structures strengthened with externally bonded CFRP-plates, in: M.C. Forde (Ed.), Proc., 7th Int. Conf. on Structural Faults and Repair, Engineering Technics Press, Edinburgh, U.K., 1997, pp. 109–118.
[66] Z.P. Bazant, P.A. Pfeiffer, Determination of fracture energy from size effect and brittleness number, ACI Mater. J. 84 (6) (1987) 463–480.
[67] M. Elices, G. Guinea, J. Planas, On the measurement of concrete fracture energy using three-point bend tests, Mater. Struct. 30 (6) (1997) 375–376.
[68] G. Guinea, J. Planas, M. Elices, Measurement of the fracture energy using three-point bend tests: Part 1-influence of experimental procedures, Mater. Struct. 25 (4) (1992) 212–218.
[69] A. Hillerborg, M. Modéer, P.E. Petersson, Analysis of crack formation and crack growth in concrete by means of fracture mechanics and finite elements, Cem. Concr. Res. 6 (6) (1976) 773–781.
[70] R.D. Recommendation, Determination of the fracture energy of mortar and concrete by means of three-point bend tests on notched beames, Mater. Struct. 18 (106) (1985) 285–290.
[71] P. Holzenkämpfer, Ingenieur Modelle Des Verbundes Geklebter Bewehrung für Betonbauteile. Ph.D. dissertation, TU Braunschweig, Germany, 1994. in German.
[72] M. Charalambides, A.J. Kinloch, Y. Wang, J.G. Williams, On the analysis of mixed-mode failure, Int. J. Fract. 54 (3) (1992) 269–291.
[73] D. Álvarez, F.J. Guild, A.J. Kinloch, B.R.K. Blackman, Partitioning of mixed-mode fracture in adhesively-bonded joints: experimental studies, Eng. Fract. Mech. 203 (2018) 224–239.
[74] X.U. Fu-quan, G. Jian-Guang, C. Yu, Bond strength between CFRP sheets and concrete FRP Compos. Civ. Eng., Elsevier Science, Oxford, U.K, 2001, pp. 357–364.
[75] J.W. Shi, H. Zhu, Z.S. Wu, G. Wu, Experimental study on bond behavior between Basalt/Hybrid FRP sheets and concrete substrates, J. Southeast Univ. 40 (3) (2010) 554–558 (in Chinese).
[76] A. Bilotta, F. Ceroni, M. Di Ludovico, E. Nigro, M. Pecce, G. Manfredi, Bond efficiency of EBR and NSM FRP systems for strengthening concrete members, J. Compos. Constr. 15 (5) (2011) 757–772.
[77] K. Liu, Computational Modeling, Experimental and Theoretical Study on Bond Behaviors of Hybrid-bonded FRP Strengthened Concrete Structures PhD thesis, City Univ. of Hong Kong, Hong Kong, 2011.
[78] K. Hunebum, M. Stijn, P. Aniello, S. Yuichi, Development of a simplified bond stress–slip model for bonded FRP-concrete interfaces, Constr. Build. Mater. 68 (14) (2014) 142–157.
[79] G. Monti, M. Renzelli, P. Luciani, FRP adhesion in uncracked and cracked concrete zones, in: Proc., 6th Int. Symp. on FRP Reinforcement for Concrete Structures (FRPRCS-6), World Scientific, Singapore, 2003, pp. 183–192.
[80] M. Savioa, B. Farracuti, D. Mazzotti, Non-linear bondslip law for FRP-concrete interface, in: Proc., 6th Int. Symp. on FRP Reinforcement for Concrete Structures, FRPRCS-6, World Scientific, Singapore, 2003, pp. 163–172.

[81] J. G. Dai and Ueda, T. Local bond stress slip relations for FRP composites-concrete interfaces. Proc., FRPRCS-6, K. H. Tan, ed., 2003, Vol. l, 143–152.
[82] T. Ueda, J.G. Dai, Y. Sato, A nonlinear bond stress-slip relationship for FRP sheet-concrete interface, in: Proc., Int. Symp. on Latest Achievement of Technology and Research on Retrofitting Concrete Structures, Japan Concrete Institute (JCI), Tokyo, Japan, 2003, pp. 113–120.
[83] J.L. Pan, Y.F. Wu, Analytical modeling of bond behavior between FRP plate and concrete, Compos. B Eng. 61 (2014) 17–25.
[84] T. Shear Tanaka, Resisting Mechanism of Reinforced Concrete Beams with CFS as Shear Reinforcement Graduation thesis, Hokkaido Univ, Hokkaido, Japan, 1996.
[85] Y. Hiroyuki, Z.S. Wu, Analysis of debonding fracture properties of CFS strengthened member subject to tension., in: Proc., 3rd Int. Symp. on Non-metallic (FRP) Reinforcement for Concrete Structures, Japan Concrete Institute, Tokyo, 1997, pp. 287–294.
[86] O. Chaallal, M.J. Nollet, D. Perraton, Strengthening of reinforced concrete beams with externally bonded fibre-reinforced-plastic plates: design guidelines for shear and flexure, Can. J. Civ. Eng. 25 (4) (1998) 692–704.
[87] Y. Yang, Q. Yue, Y. Hu, Experimental study on bond performance between carbon fiber sheets and concrete, J. Build. Struct. 22 (3) (2001) 36–42 (in Chinese).
[88] Japan Concrete Institute (JCI), Technical report of technical committee on retrofit technology, Proc., Int. Symp. on Latest Achievement of Technology and Research on Retrofitting Concrete Structures, Japan Concrete Institute (JCI), Tokyo, Japan, 2003.